

**AFRL-ML-WP-TR-2004-4142**

**NONDESTRUCTIVE EVALUATION  
(NDE) TECHNOLOGY INITIATIVES  
PROGRAM (NTIP)**

**Delivery Order 0030: Magnetoresistive Sensors  
for Eddy Current Imaging Nondestructive  
Evaluation (NDE)**



**By:**

**Raymond D. Rempt**

**Boeing Company**

**Phantom Works**

**P.O. Box 3707, MC 2T-50**

**Seattle, WA 98124-2207**

**For:**

**Universal Technology Corporation**

**1270 North Fairfield Road**

**Dayton, OH 45432-2600**

**JULY 2003**

**Final Report for 15 February 2002 – 31 July 2003**

**Approved for public release; distribution is unlimited.**

**STINFO FINAL REPORT**

**MATERIALS AND MANUFACTURING DIRECTORATE  
AIR FORCE RESEARCH LABORATORY  
AIR FORCE MATERIEL COMMAND  
WRIGHT-PATTERSON AIR FORCE BASE, OH 45433-7750**

## NOTICE

WHEN GOVERNMENT DRAWINGS, SPECIFICATIONS, OR OTHER DATA ARE USED FOR ANY PURPOSE OTHER THAN IN CONNECTION WITH A DEFINITELY GOVERNMENT-RELATED PROCUREMENT, THE UNITED STATES GOVERNMENT INCURS NO RESPONSIBILITY OR ANY OBLIGATION WHATSOEVER. THE FACT THAT THE GOVERNMENT MAY HAVE FORMULATED OR IN ANY WAY SUPPLIED THE SAID DRAWINGS, SPECIFICATIONS, OR OTHER DATA, IS NOT TO BE REGARDED BY IMPLICATION OR OTHERWISE IN ANY MANNER CONSTRUED, AS LICENSING THE HOLDER OR ANY OTHER PERSON OR CORPORATION, OR AS CONVEYING ANY RIGHTS OR PERMISSION TO MANUFACTURE, USE, OR SELL ANY PATENTED INVENTION THAT MAY IN ANY WAY BE RELATED THERETO.

THIS REPORT HAS BEEN REVIEWED BY THE OFFICE OF PUBLIC AFFAIRS (ASC/PA) AND IS RELEASABLE TO THE NATIONAL TECHNICAL INFORMATION SERVICE (NTIS). AT NTIS, IT WILL BE AVAILABLE TO THE GENERAL PUBLIC, INCLUDING FOREIGN NATIONS.

THIS TECHNICAL REPORT HAS BEEN REVIEWED AND IS APPROVED FOR PUBLICATION.

/s/

THOMAS J. MORAN, Project Engineer  
Nondestructive Evaluation Branch  
Metals, Ceramics & NDE Division

/s/

JAMES C. MALAS, Chief  
Nondestructive Evaluation Branch  
Metals, Ceramics & NDE Division

/s/

GERALD J. PETRAK, Assistant Chief  
Metals, Ceramics & NDE Division  
Materials & Manufacturing Directorate

IF YOUR ADDRESS HAS CHANGED, IF YOU WISH TO BE REMOVED FROM OUR MAILING LIST, OR IF THE ADDRESSEE IS NO LONGER EMPLOYED BY YOUR ORGANIZATION, PLEASE NOTIFY, AFRL/MLLP, WRIGHT-PATTERSON AFB OH 45433-7817 TO HELP US MAINTAIN A CURRENT MAILING LIST.

COPIES OF THIS REPORT SHOULD NOT BE RETURNED UNLESS RETURN IS REQUIRED BY SECURITY CONSIDERATIONS, CONTRACTUAL OBLIGATIONS, OR NOTICE ON A SPECIFIC DOCUMENT.

<b>REPORT DOCUMENTATION PAGE</b>				<i>Form Approved</i> <i>OMB No. 0704-0188</i>				
The public reporting burden for this collection of information is estimated to average 1 hour per response, including the time for reviewing instructions, searching existing data sources, gathering and maintaining the data needed, and completing and reviewing the collection of information. Send comments regarding this burden estimate or any other aspect of this collection of information, including suggestions for reducing this burden, to Department of Defense, Washington Headquarters Services, Directorate for Information Operations and Reports (0704-0188), 1215 Jefferson Davis Highway, Suite 1204, Arlington, VA 22202-4302. Respondents should be aware that notwithstanding any other provision of law, no person shall be subject to any penalty for failing to comply with a collection of information if it does not display a currently valid OMB control number. <b>PLEASE DO NOT RETURN YOUR FORM TO THE ABOVE ADDRESS.</b>								
<b>1. REPORT DATE (DD-MM-YY)</b> July 2003		<b>2. REPORT TYPE</b> Final		<b>3. DATES COVERED (From - To)</b> 02/15/2002 – 07/31/2003				
<b>4. TITLE AND SUBTITLE</b> NONDESTRUCTIVE EVALUATION (NDE) TECHNOLOGY INITIATIVES PROGRAM (NTIP) Delivery Order 0030: Magnetoresistive Sensors for Eddy Current Imaging Nondestructive Evaluation (NDE)				<b>5a. CONTRACT NUMBER</b> F33615-97-D-5271-0030				
				<b>5b. GRANT NUMBER</b>				
				<b>5c. PROGRAM ELEMENT NUMBER</b> 62102F				
<b>6. AUTHOR(S)</b> Raymond D. Rempt				<b>5d. PROJECT NUMBER</b> 4349				
				<b>5e. TASK NUMBER</b> 40				
				<b>5f. WORK UNIT NUMBER</b> 01				
<b>7. PERFORMING ORGANIZATION NAME(S) AND ADDRESS(ES)</b> <table style="width: 100%; border: none;"> <tr> <td style="width: 50%; vertical-align: top;"> <b>By:</b>            Boeing Company            Phantom Works            P.O. Box 3707, MC 2T-50            Seattle, WA 98124-2207         </td> <td style="width: 50%; vertical-align: top;"> <b>For:</b>            Universal Technology Corporation            1270 North Fairfield Road            Dayton, OH 45432-2600         </td> </tr> </table>				<b>By:</b> Boeing Company Phantom Works P.O. Box 3707, MC 2T-50 Seattle, WA 98124-2207	<b>For:</b> Universal Technology Corporation 1270 North Fairfield Road Dayton, OH 45432-2600	<b>8. PERFORMING ORGANIZATION REPORT NUMBER</b>		
<b>By:</b> Boeing Company Phantom Works P.O. Box 3707, MC 2T-50 Seattle, WA 98124-2207	<b>For:</b> Universal Technology Corporation 1270 North Fairfield Road Dayton, OH 45432-2600							
<b>9. SPONSORING/MONITORING AGENCY NAME(S) AND ADDRESS(ES)</b> Materials and Manufacturing Directorate Air Force Research Laboratory Air Force Materiel Command Wright-Patterson AFB, OH 45433-7750								
<b>10. SPONSORING/MONITORING AGENCY ACRONYM(S)</b> AFRL/MLLP				<b>11. SPONSORING/MONITORING AGENCY REPORT NUMBER(S)</b> AFRL-ML-WP-TR-2004-4142				
<b>12. DISTRIBUTION/AVAILABILITY STATEMENT</b> Approved for public release; release is unlimited.								
<b>13. SUPPLEMENTARY NOTES</b> Report contains color.								
<b>14. ABSTRACT</b> Development and performance of a 64-element imaging array for use in eddy current NDE for aircraft using anisotropic magnetoresistive sensors (AMR) is described and discussed. Among the design issues are flaw field modeling, excitation current configuration, and orientation and configuration of the sensors themselves. The array can rapidly find cracks of the order of 0.2 inch under 0.3 inch or more of metal. This is a good improvement compared to conventional eddy current means, as it enables the scanning of large areas of aircraft surface, thus potentially eliminating the necessity to examine each fastener hole individually by hand. The intention is to mount the array on the MAUS platform for depot inspections, and possibly some fieldwork.								
<b>15. SUBJECT TERMS</b> eddy current, anisotropic magnetoresistive sensors (AMR), MAUS, NDE								
<b>16. SECURITY CLASSIFICATION OF:</b> <table style="width: 100%; border: none;"> <tr> <td style="width: 33%;"><b>a. REPORT</b> Unclassified</td> <td style="width: 33%;"><b>b. ABSTRACT</b> Unclassified</td> <td style="width: 33%;"><b>c. THIS PAGE</b> Unclassified</td> </tr> </table>			<b>a. REPORT</b> Unclassified	<b>b. ABSTRACT</b> Unclassified	<b>c. THIS PAGE</b> Unclassified	<b>17. LIMITATION OF ABSTRACT:</b> SAR		<b>18. NUMBER OF PAGES</b> 30
<b>a. REPORT</b> Unclassified	<b>b. ABSTRACT</b> Unclassified	<b>c. THIS PAGE</b> Unclassified						
<b>19a. NAME OF RESPONSIBLE PERSON (Monitor)</b> Tom Moran			<b>19b. TELEPHONE NUMBER (Include Area Code)</b> (937) 255-9800					
			(937) 255-9800					

## TABLE OF CONTENTS

1.0	SUMMARY .....	1
2.0	INTRODUCTION .....	1
3.0	METHODS, ASSUMPTIONS AND PROCEDURES .....	2
3.1	Modeling .....	2
3.2	Drive Current Configuration .....	7
3.3	Sensor Spacing and Placement .....	8
3.4	Display Options .....	12
3.5	Array Head .....	12
4.0	RESULTS AND DISCUSSION .....	14
4.1	Thick Parts with Deep Flaws .....	14
5.0	CONCLUSIONS .....	19

## LIST OF FIGURES

Figure 1.	Setup for current and field modeling. 31 parallel wires are used to excite a “sheet of current” on the surface of the sample. The crack has 3 possible orientations. ....	2
Figure 2.	Induced eddy current density from 31 excitation wires above the sample.....	3
Figure 3.	Field components with crack subtracted from those without crack. ....	3
Figure 4.	Field differences for a crack 5 times longer than that of figure 4.....	4
Figure 5.	Different fields, using conductive ribbons for excitation instead of wires.....	5
Figure 6.	Field differences for the sample with fastener hole and crack, with those due to a featureless substrate of the same size subtracted out, thus simulating what is seen with the array.....	6
Figure 7.	Configuration of 64-element array per the spacing conditions: The inter-sensor spacing is 0.0125 inch, normal to the scan direction.....	8
Figure 8.	Numeration of sensors: Scan direction is to the right, and view is from the top. Strings are essentially parallel to the scan direction, with the angle exaggerated to demonstrate the staggering of the strings. ....	9
Figure 9.	X gradient difference and presentation scheme. There is a blank row at the location of every 8 <sup>th</sup> sensor. This must be maintained in the image or else the “picture” that is presented will not represent the sample being scanned. ....	10
Figure 10.	Y Gradient difference calculation and presentation scheme: Since the blank rows all occur contiguously, the subsequent stanza can be scanned over the portion that was blank, leaving no blank space in the scan, except at the top of the last stanza. ....	11
Figure 11.	64-element array, shown without its metal shield, with eight strings of sensors and 8x19 pins protruding through the Delryn mounting mandrel. ....	12
Figure 12.	64-element mounted on scanning bridge. Note all wires appear in bundle at the rear of the metal shield enclosure of the head.....	13
Figure 13.	Scanning surface of 64-element array head. (Note: The ribbon like traces, which launch the unidirectional current sheet into the sample. The angle between the string orientation and the scan direction can also be seen through the Mylar excitation unit, showing its thinness. The return traces are located at the top and bottom of the unit, and are bunched more closely together than the excitation traces.).....	14
Figure 14.	Sample used for initial performance demonstration of 64-element array: (Note: The wider upper layer has fastener holes with countersinks. The narrower lower layer has holes without countersinks. The four lines represent through cracks in the lower layer. The cracks on the second hole from the left are 0.300” each, and those on the fourth hole from the left are 0.200” each.).....	15
Figure 15.	64-element scan of sample shown in Figure 14: The array is operated in magnetometer mode. The sample is rotated 90 degrees from its image in the previous figure. The 0.300 and 0.200 flaws are easily seen in both images, but the contrast squeezed image on the right picks out the inside	

	flaws slightly better. All of the fastener holes are detected as a pair of crescents. Only two of the fastener holes have flaws. ....	16
Figure 16.	Sample used to demonstrate functionality of field gradient as a viable scanning parameter. All of the flaws are 0.600” in length, and some are only on one side of the fastener hole; otherwise, the sample is identical to that of Figure 14.....	17
Figure 17.	Gradiometer scan image of the sample in Figure 16: All of the cracks are seen, as indicated by the arrows, and the fastener holes are not pronounced. This scan was not processed in any way, but is shown as taken.....	18
Figure 18.	Wider gradiometer scan of the same sample, rotated by ninety degrees: Arrows show flaws, and the bands at sides show the edge of the narrower lower layer. ....	18

# **MAGNETORESISTIVE SENSORS FOR EDDY CURRENT IMAGING NDE**

## **FINAL REPORT**

**July 31, 2002**

This report covers effort for the Magnetoresistive sensors for eddy-current imaging NDE Contract, Contract number 02-S437-030-C1, commencing on February 15<sup>th</sup> 2002, and finishing July 31<sup>st</sup> 2003.

### **1.0 SUMMARY**

The mission of this contract was to build and evaluate an imaging array using magnetoresistive sensors, and to evaluate certain operational and conceptual parameters associated with such an array, to come up with an initial preferred and recommended design for an array for use in Air Force depot inspections. The work done on this contract constituted the natural continuation of work done under previous contract number 00-S437-013-C2, entitled "Scanning with Magnetoresistive Sensors for Subsurface Corrosion". The array was built and evaluated using Anisotropic Magnetoresistive (AMR) sensors. A cursory and preliminary study to determine the sensibility and attractiveness of incorporating other types of MR sensors, including Giant Magnetoresistive (GMR) sensors, and Spin Dependent Tunneling (SDT) sensors into such an array was also performed.

### **2.0 INTRODUCTION**

Air Force Research Lab (AFRL) has had interest in exploiting the advantages offered by MR sensors for a number of years. Boeing's work started in 1995, and has continued to the present, with internal funding, as well as funding from the two contracts mentioned above. During the initial period of Boeing's work, AMR sensors were characterized, and evaluated in both magnetometer and gradiometer configurations. It became clear that one of the more attractive applications of these sensors would be in an array which would permit rapid scanning of areas of interest on an aircraft such as fuselage lap joints, or wing root areas. Currently, procedures call for separate inspections of each individual fastener, which is labor intensive, time-consuming, and expensive. An array capable of giving real time images of the subsurface condition of aircraft structure as it is scanned over the surface, would be of significant value. The images produced by the array could be looked at in real time, and then only those fasteners whose images showed "areas of interest" would need to be further inspected. This contract is geared to demonstrating that such an array can be built, and to commencing with the derivation of its requirements and design.

Magnetoresistive sensors have been known for several decades. They are commonly used in the magnetic media/recording industry. In the early 90's, the high performance sensors were first developed by Kodak, and were of the anisotropic variety. Kodak later sold the rights for the AMR sensors to San Diego Magnetics, from whom Boeing has purchased sensors, both singly, and in arrays. Later, both the GMR and the SDT sensors emerged. NVE Corporation, which makes both the GMR and the SDT sensors, has been under contract to AFRL to direct NDE efforts with these sensors, with Albany Electronics sub-contracted to do the actual NDE research. Boeing is in contact with both of these entities. It is envisioned, that the preferred array, which will be the continuation of the work under this contract, may include one or more of the three types of sensors.

The first application of the array will be to scan appropriate regions of aircraft to inspect for deeply lying flaws. The array will be deployed with a currently used Air Force depot platform such as the MAUS.

### **3.0 METHODS, ASSUMPTIONS AND PROCEDURES**

#### **3.1 Modeling**

In order to successfully arrive at the requirements for the array, a good understanding of the eddy-current situation is necessary. We have modeled eddy currents launched into the surface of an aluminum substrate, and the resultant fields produced. We have done this for the full volume of the sample shown in figure 1, using Microwave Studios Maxwell Equation Solver. The excitation current launched into the surface of the sample is in the form of a unidirectional "sheet" comprised of parallel wires each of which has the same current. The sample consists of two 0.25" thick plates with a 5/16" diameter fastener hole, having a countersunk head. There is a "crack" which is 0.25" long, all the way through the lower plate, which can be oriented parallel to either of the plate sides, or along the diagonal. The crack is 0.008" wide.

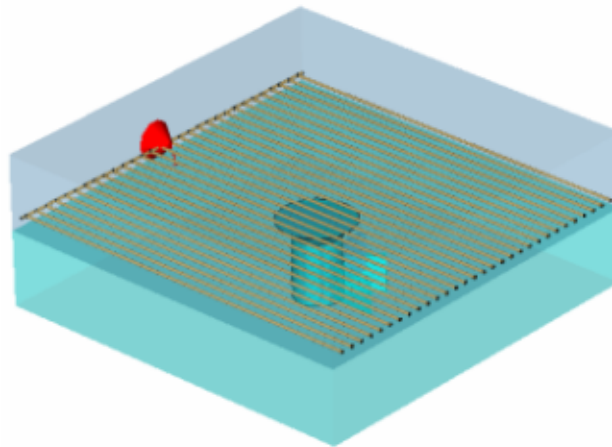


Figure 1. Setup for current and field modeling. 31 parallel wires are used to excite a "sheet of current" on the surface of the sample. The crack has 3 possible orientations.



The distribution of resultant current density is shown in figure 2.

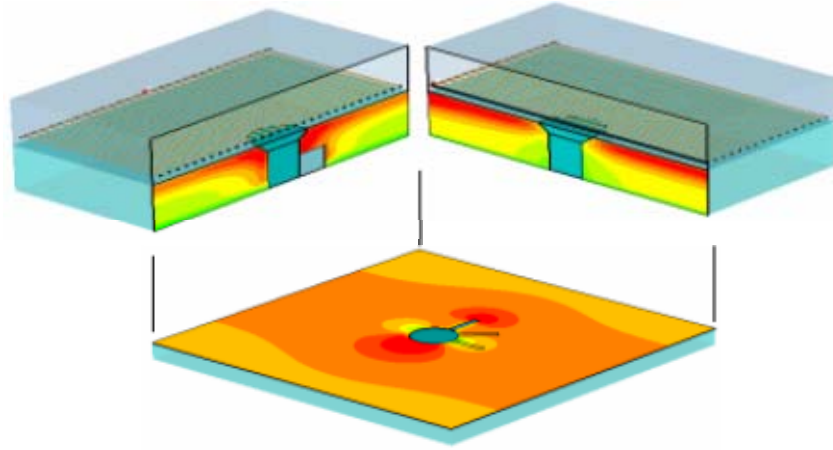


Figure 2. Induced eddy current density from 31 excitation wires above the sample.

In this figure, the three orientations of the crack are shown, but two are filled with aluminum for purposes of this calculation. The crack orientation that is normal to the launched current direction is filled with air, and is therefore the one that gives rise to the distribution shown. Note the more concentration of the currents at the tip of the crack, and the opposite side of the fastener hole. In figure 3, the magnetic fields are calculated for the full volume of the sample. Those arising from the sample with no crack are subtracted from those with the crack oriented along the Y direction. The current is launched in the X direction, and Z is normal to the surface of the sample.

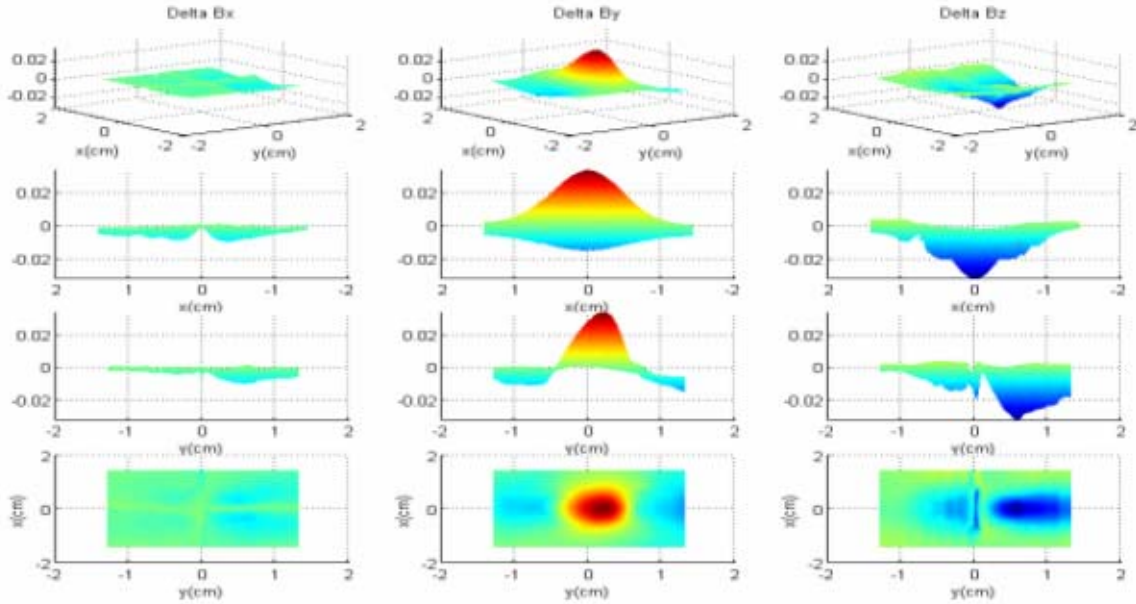


Figure 3. Field components with crack subtracted from those without crack.

The plots are shown in 3-dimension along the top row, with  $B_x$  along the current direction, by the in-plane component normal to the current but parallel to the crack, and  $B_z$  normal to the plane of the sample. The second row shows the plot with the x-axis as abscissae, and the third row shows the plot with the y-axis as abscissae. The bottom row shows the corresponding “C-scans”. In all scans shown, the crack is at “3 o’clock”, and in the C-scans, the X-axis is compressed, as can be seen in by the rivet heads represented by ellipses as shown in figures 4 and 5. It comes as no surprise that the X component of the field is very small, as it is parallel to the current. This is clear by looking at the left column of plots. Inspection of the central and right hand columns reveals that the Y and Z components are roughly the same magnitude, but the Z component does a better job of locating the crack. Figure 4 shows the same set of plots, but for a crack, which is five times longer than the one in figure 3.

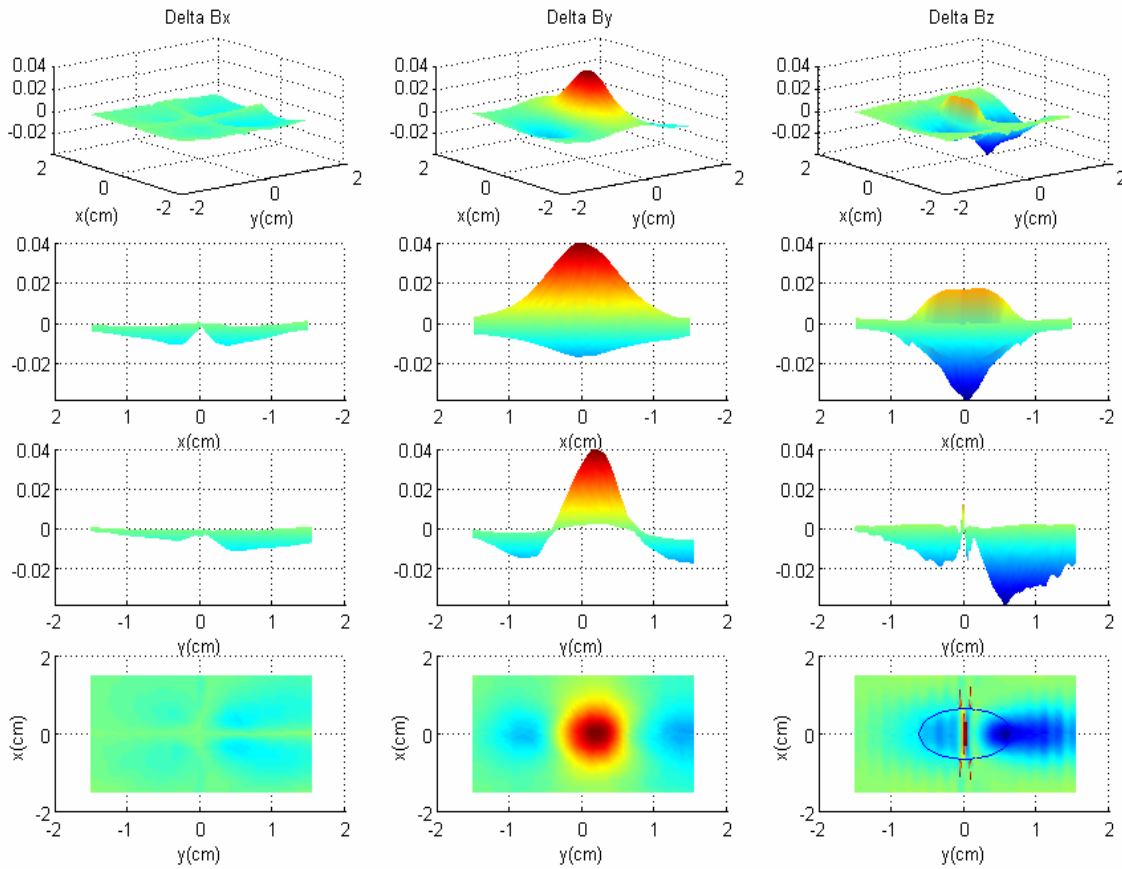


Figure 4. Field differences for a crack 5 times longer than that of figure 4.

The response to the larger crack is larger, as would be expected. The small spike at the origin in the Z component plot is due to the placement of the wires, and the fact that high mesh point densities for calculation were placed in the region of the crack and the fastener hole, but not all over the upper surface where the wires are. The spike is therefore an “artifact” of the modeling, rather than a true response to the physics. In general, it is found that for the current injected

along X, the field differences along X are far smaller than those along Y or Z. The Z component is more useful in locating the crack than the Y component. Also, from additional modeling, it is concluded that the response to the crack is far more dependent on the length of the crack, than on its width. The modeling performed under the contract was reasonably exhaustive, with only the general results stated here. Figure 5 shows the field differences for a crack that is 5 times that of figure 3, and twice as wide. In this figure, the excitation consisted of a series of conducting ribbons rather than wires, as that is what could conveniently be built for actual operation of the array.

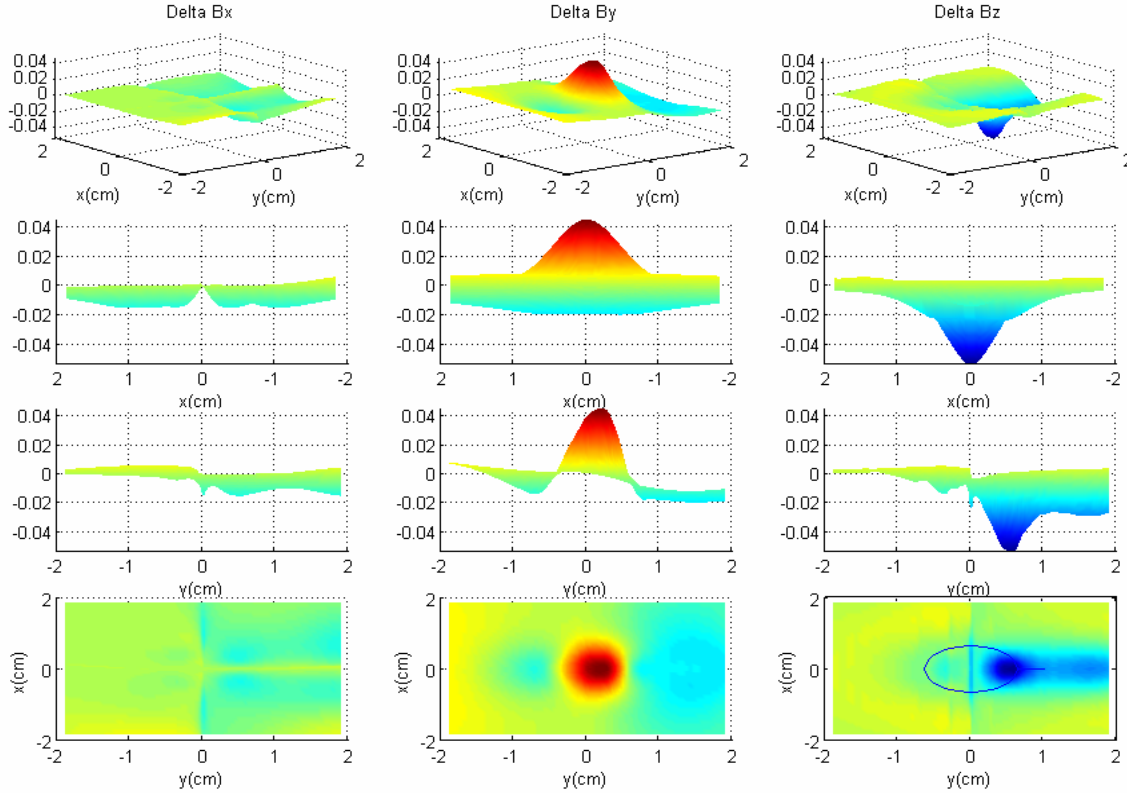


Figure 5. Different fields, using conductive ribbons for excitation instead of wires.

It is easy to see that there is no significant difference for the field differences, compared to those resulting from using wires for the excitation.

In practice, of course, it is not possible to subtract the fields for the case of a flawless sample from those of a sample containing a flaw. The procedure by which the array is “zeroed”, is to place it on a large plate of sufficiently thick aluminum, and then to add an offset to each of the sensors to bring its output to zero volts. Taking data after this procedure essentially amounts to subtracting the data of a featureless plate from that of the sample being tested. It is therefore a straightforward proposition to model this difference, and thus predict what should be seen in the laboratory. Figure 6 shows a plot of this difference. The flaw is seen by noticing that the negative peak in the Z component dips down a bit further on the right side, where the flaw is,

than on the left, where there is no flaw no crack. This is the type of feature that we look for in the lab, and later in the field, when performing an inspection. The C-scan along the bottom row shows this as well, with a larger dark region on the right than on the left.

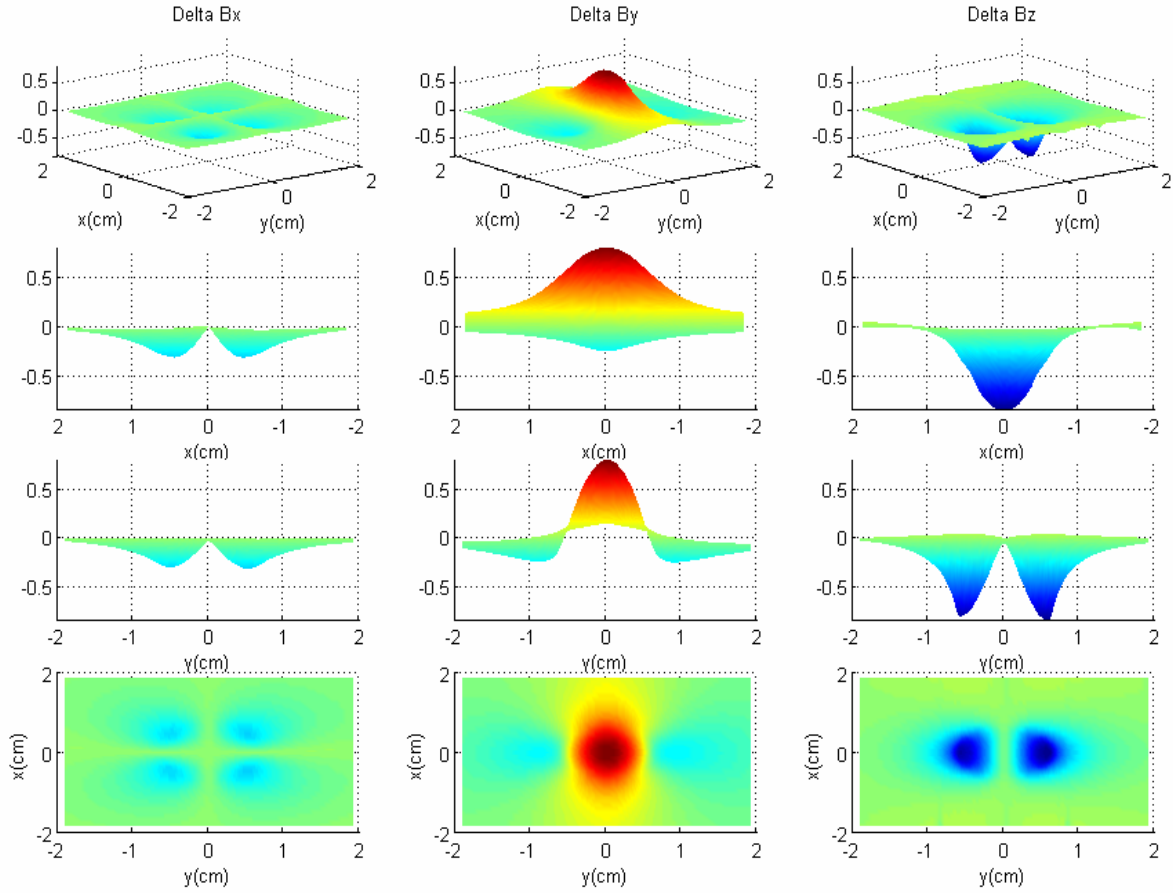


Figure 6. Field differences for the sample with fastener hole and crack, with those due to a featureless substrate of the same size subtracted out, thus simulating what is seen with the array.

In this case, which is very much like what we see using the array, the Y component does not help in locating the crack, or in even seeing that there is one. The Z component is more pronounced over the region of the crack.

In general, then, we have made the following generalized conclusions from modeling performed during the program. The Y and Z component responses to features in the sample are far greater than those of the X component. The Z component is better at locating the features, and the features depend more on the length of the crack, than the width, as long as the crack is wide enough to present a real conduction discontinuity to the injected eddy currents. In addition, some modeling was done for cases with the launched currents parallel to the long dimension of the crack. For these it was all but impossible to see the crack at all. This is not surprising, and for this reason, we show none of the results for these cases.

### 3.2 Drive Current Configuration

Historically, inspection of aircraft structure has been performed with probes using a circular coil injecting a circularly symmetric current into the sample. This is okay for a single sensor located at the center of the fastener hole, or even offset from that center. But if a number of sensors are desired so as to act like an array, then the effective field that each one experiences is a function of position inside the circular coil used as a launcher. The symmetry then becomes an adversary rather than an advocate. In addition, there would either be many drive coils required so that each sensor could have its own coil, or a very large and tremendously high current coil surrounding all of the sensors. Residual launch fields would be a problem with this geometry as well. If efficient large area scanning is desired, the circularly symmetrical currents will not fill the bill, since the circular symmetry only makes sense when directly over, and concentric with the fastener hole. For this reason, we have used a launch current configured as a “sheet”.

The sheet of current is realized by a number of ribbons of conductor, which are actually traces on a circuit board, all carrying the same current, in the same direction. This is made possible by laying the traces as part of one continuous solenoid, with the return traces on the outsides of the board. This provides a substantial region of the board with traces that all carry the same unidirectional current.

Even though the traces are all carrying the same current, there is a residual field effect that increases as the distance from the center of symmetry of the conducting traces. The net result of this effect is that the sensors that are located further from the center have a reduced dynamic range, because the residual field brings the operating point of those sensors closer to its nonlinear region. We have looked into ways of reducing this, but have not come up with a clear answer at this point. Increasing the size of the total board with the excitation traces, is the only way we have seen to date, as it places the entire array closer to the center of symmetry of the traces, and therefore reduces the amount of residual field that any given sensor experiences.

We have made up current sheet launchers as described above that are traces on thin and flexible Mylar rather than the normal G-10 circuit board material. Two such launchers can be mounted with adhesive on top of each other, but oriented at right angles with respect to one another, and then affixed with a suitable adhesive to a rigid substrate made of a material such as Delryn. This rigid substrate has a port machined through it, so that the array of sensors can be mounted in the port, near to the launchers as is reasonably achievable, to ensure that the sensors are as close to the sample as possible. One can quickly see that with such an arrangement of two launchers, the direction of the current in the plane of the sample may be arbitrarily set, simply by driving each of the launchers with the appropriate amplitude.

As a final variation on the two-launcher arrangement, driving the launchers with currents that are ninety degrees apart in phase has the effect of causing the current sheet to “spin”. This ensures that the current interacts with any given feature or flaw in a manner which maximizes the resulting signature. Such an arrangement would be of more than simple academic interest to the NDE community.

### 3.3 Sensor Spacing and Placement

Measurements made in previous years, have shown that it is acceptable to set the spacing between adjacent sensors to be such that the response of the same feature to a given sensor does not diminish down to less than 97.5% of its value. This value is chosen so that a reasonably high-resolution image is produced by the array. The value could be relaxed, resulting in a wider array, and certainly there is no loss of generality in doing so, but the resulting image will be less “attractive” to look at.

The sensors are diced from the silicon wafer on which they are fabricated. The spacing between the adjacent sensors on the wafer is 1454 microns. Since each of the sensors needs to be surrounded with a bias coil, every other sensor had to be “sacrificed”, and the resulting spacing between sensors on the wafer was therefore 2908 microns, or 0.1145 inch.

The array is made up of 8 strings of 8 sensors each, spaced as described above. Each of the strings is composed of a section diced from the wafer that had 15 of the sensors, with every other sensor cut out to permit installation of the coils. In order to produce a linear array, the strings were placed at an angle of 6.3 degrees with respect to the scan direction. This is shown in figure 7.

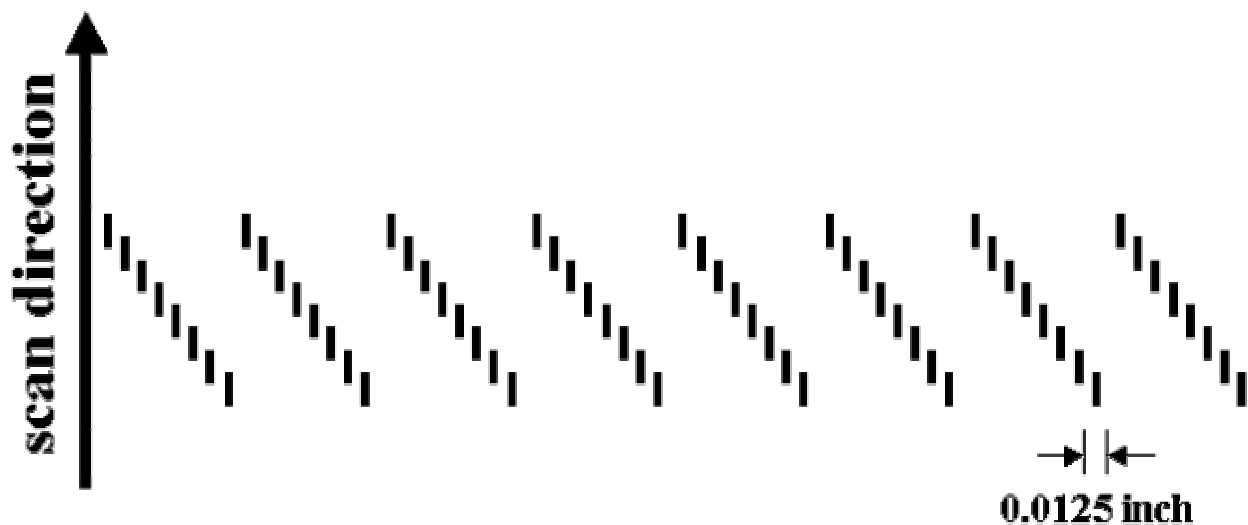


Figure 7. Configuration of 64-element array per the spacing conditions: The inter-sensor spacing is 0.0125 inch, normal to the scan direction.

Data are collected in a staggered fashion, so that the images produced appear correctly. This requires that the scan lines be longer than the actual imaged area by the length of the array, which is about 0.8 inch. When the array is indexed between scan passes, the indexing amount is the width of the whole array. Of course, in order to see the effect of the 6.3-degree angle, it has been greatly exaggerated in figure 7. It is shown at about 30 degrees, although it is only 6.3 and

the strings of sensors are really much closer to being parallel to the scan direction than the figure would indicate.

Since the scan direction is defined to be the “X” direction in all of the software, there are two designations for in-plane field gradients, which are “X”, and “Y” respectively. When the array is being used to produce gradient images, they are called “X” if the subtraction occurs between adjacent sensors in the same string, since that is essentially along X. If the array is switched so that the subtraction occurs between sensors in adjacent strings, then that gradient is designated as “Y”. Figures 8, 9, and 10 serve to show how the sensors are numbered and how these gradients are plotted.

For the X gradient case, there are only 7 outputs for each string, resulting in a total of 56 outputs. These outputs are 1-2, 2-3, 3-4, 4-5, 5-6, 6-7, and 7-8. Since it makes no sense to subtract number 1 from number 8, there is a blank line at the end of each string for this case. For the Y gradients, the outputs are 9-1, 10-2, 11-3, and so forth. Since it makes no sense to subtract sensors in the last string from those in the first, there is a blank that is 8 sensors wide at the end of each stanza. As in the X gradient case, this scan has 56 channels as well.

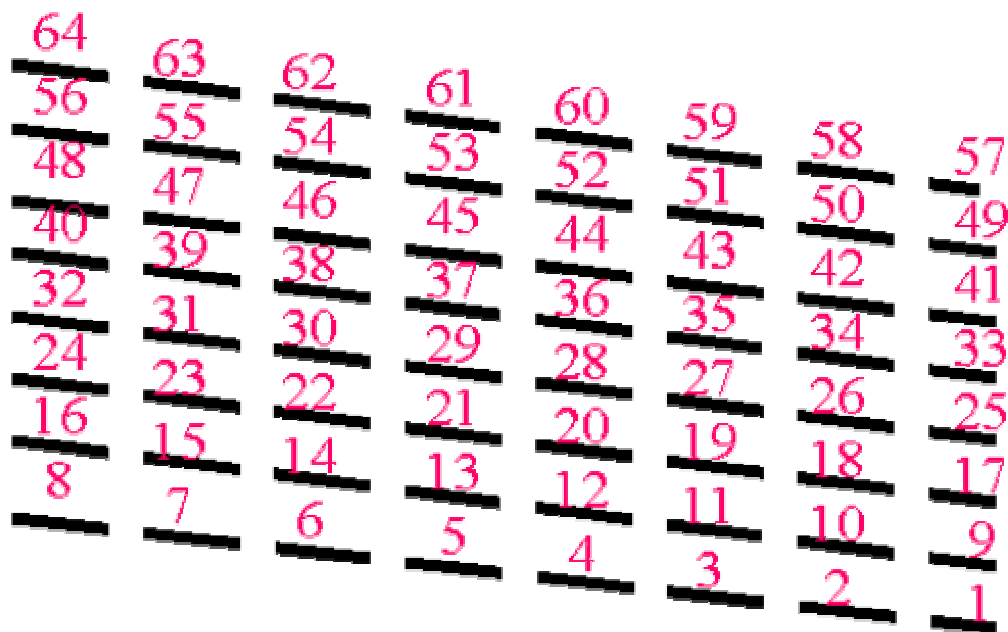


Figure 8. Numeration of sensors: Scan direction is to the right, and view is from the top. Strings are essentially parallel to the scan direction, with the angle exaggerated to demonstrate the staggering of the strings.

Figure 9 shows how the gradients are calculated and plotted for the “X gradient” case. This is the case where adjacent sensors in the same string are subtracted to produce the gradient values.

It can be seen that there is a blank strip corresponding to every eighth sensor location. When the data are collected, and the image presented, there is a blank line in each of these locations, since no data were taken from them.

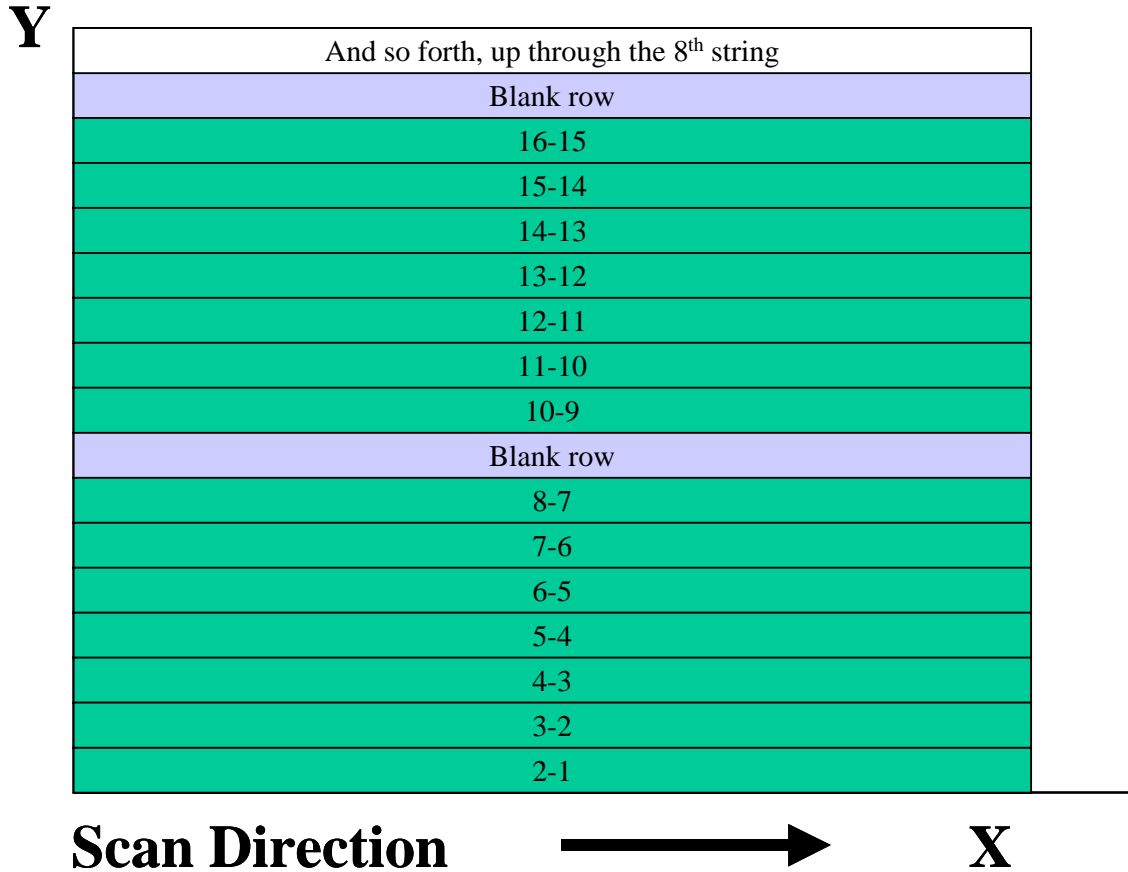


Figure 9. X gradient difference and presentation scheme. There is a blank row at the location of every 8<sup>th</sup> sensor. This must be maintained in the image or else the “picture” that is presented will not represent the sample being scanned.

For the Y gradient, the situation is much different. Each difference is between the corresponding sensors in adjacent strings. Therefore, the blank space does not occur until the location of the eighth string, since it is the one that has no “partner” from which it can be subtracted.

The images for the Y gradient, though can be continuous and un-interrupted, since when the scan is done, the array can be indexed only by an amount necessary to cover the actual data, and the blank rows are then scanned over by the next scan line. The only blank portion in the image will then be at the top of the very last stanza, where there will be no data for the final swath of 8 sensors width. In this way, the Y gradient images look like a single scan with no artifacts of the gradiometry, whereas the X gradient has the lines at every 8<sup>th</sup> sensor location.



The Y gradient difference calculations and resulting image format is shown in Figure 10. For the sake of brevity, most of the difference swaths have been omitted, and simply replaced by “etc”.

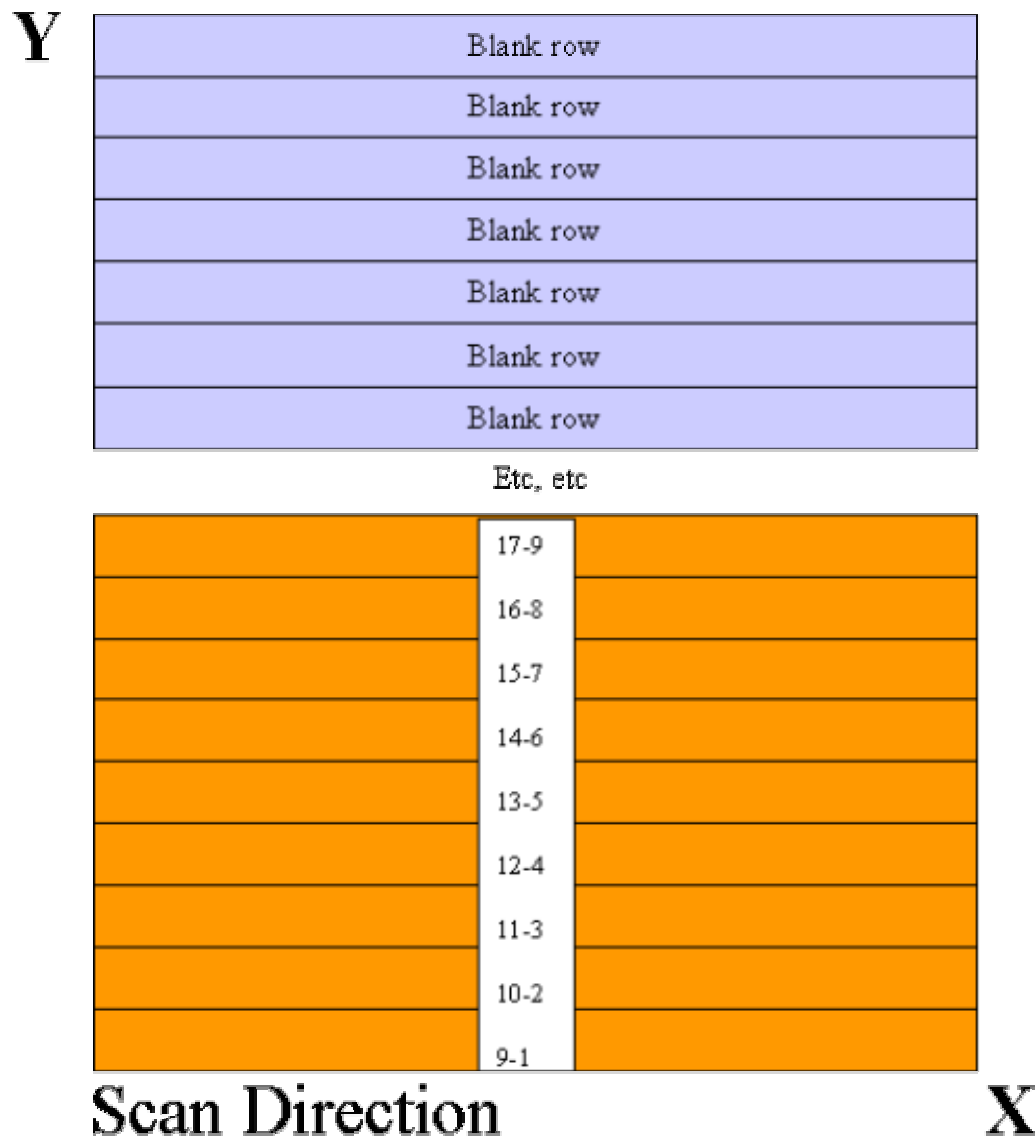


Figure 10. Y Gradient difference calculation and presentation scheme: Since the blank rows all occur contiguously, the subsequent stanza can be scanned over the portion that was blank, leaving no blank space in the scan, except at the top of the last stanza.

### 3.4 Display Options

Since the output of the sensors is processed with a lock-in amplifier, there are two channels simultaneously available from each sensor. These are the in phase and the quadrature channels. Data from each of the channels are simultaneously collected and processed to produce two images. It is possible, therefore, to select the two images that will be displayed as the scan is performed. These can be two images from 64-channel magnetometer data, or two images of 56-channel gradiometer data, or one 64 and one 56 channel image. Due to the complexity of switching, it is not possible to simultaneously see an X and a Y gradient. Both gradient channels must be the same, either both X, or both Y.

### 3.5 Array Head

The sensors are configured in eight strings of eight within the head enclosure. There is a Delryn mandrel, through which the pins from each of the strings are inserted, that holds the whole head together, and provides a rigid base for the excitation current launcher. Each of the strings requires 19 pins. These are two for the bridge bias buses, a common ground for all of the feed back coils, and 8 pins each for sensor output and feedback coil. The way in which the sensors are spaced, requires that the pins require a greater physical spread than the sensors, so each string is about 2 inches long, with the sensors occupying only the central 0.8 inch or so of the total. A picture of the head is shown in Figure 11. The eight strings are easily seen, along with the rows of 19 pins above each of the strings.



Figure 11. 64-element array, shown without its metal shield, with eight strings of sensors and 8x19 pins protruding through the Delryn mounting mandrel.

The head is enclosed in an aluminum shield, which is shown in Figure 12. In this figure, the entire array head is mounted on an XY scanning bridge. All of the leads going to the array are clearly seen in the figure. This gives an idea of the physical scope and scale of the array.

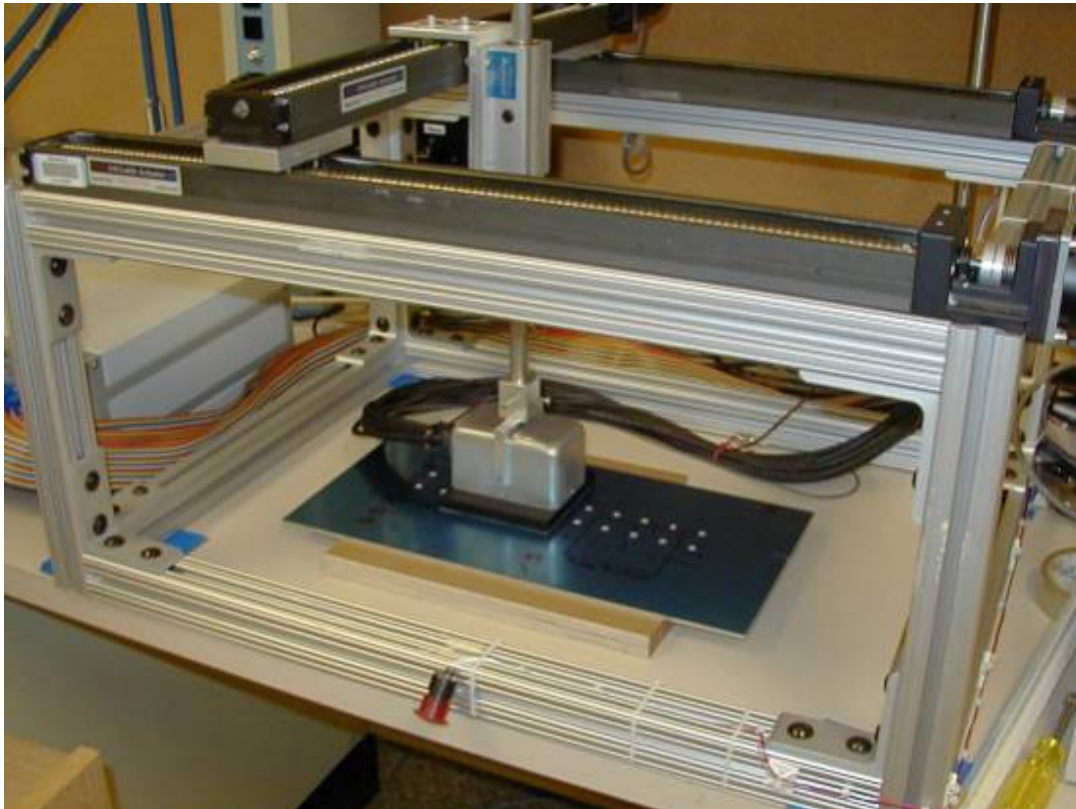


Figure 12. 64-element mounted on scanning bridge. Note all wires appear in bundle at the rear of the metal shield enclosure of the head.

The surface that contacts the sample is shown in Figure 13. It is possible to see the ribbon-like traces that comprise the excitation current launcher. The angle between the orientation of the strings of sensors and the scan direction is also evident in this photo. The fact that these two details can be picked out shows how thin the total launcher is, yet it is remarkably robust. The traces are covered over with a  $\sim 0.003''$  thick Mylar tape. This tape has two functions. First, it prevents shorting between the traces when they contact the metallic surface of the sample; and second, it provides a smooth surface with can glide more easily over the surface of the sample with which it is contact.

The physical dimensions of the “footprint” of the scanning head as shown are approximately 4” by 4”. Those of the envisioned prototype array for field evaluation will be somewhat larger. Dimensions of this range should pose no problem for mounting on the MAUS.



Figure 13. Scanning surface of 64-element array head. (Note: The ribbon like traces, which launch the unidirectional current sheet into the sample. The angle between the string orientation and the scan direction can also be seen through the Mylar excitation unit, showing its thinness. The return traces are located at the top and bottom of the unit, and are bunched more closely together than the excitation traces.)

## **4.0 RESULTS AND DISCUSSION**

### **4.1 Thick Parts with Deep Flaws**

Since the primary goal of the program is to develop a reliable and easy to use imaging scanner that reliably detects deeply lying flaws, we started evaluating the performance of the array for these types of features. We have not looked at thin types of samples, because we are reasonably certain that the array can be easily “tuned” to do such a task, as was demonstrated when we previously studied a number of such samples with one and then two, and then 8 of the sensors. It will involve merely adjusting the frequency, detection phase point, excitation current amplitude, and data collection configuration. We do not anticipate any difficulty in doing this.

We have started to investigate the array performance with thicker parts. These are both standards, as well as portions excised from actual aircraft. We initially investigated a sample that simulates a 767 wing root area. It consists of a 0.350" aluminum skin, covering a 0.395" thick doubler underneath. The sample has two rows of 0.375" fastener holes, which are staggered with respect to one another, with counter sunk heads. The holes are unfilled. In one of the rivet holes, there are 0.300" through cracks emanating from the 12 o'clock and 6 o'clock positions. Another hole has two similar cracks, but they are only 0.200" long each. All of the cracks are 0.008" wide. The sample is shown in Figure 14.

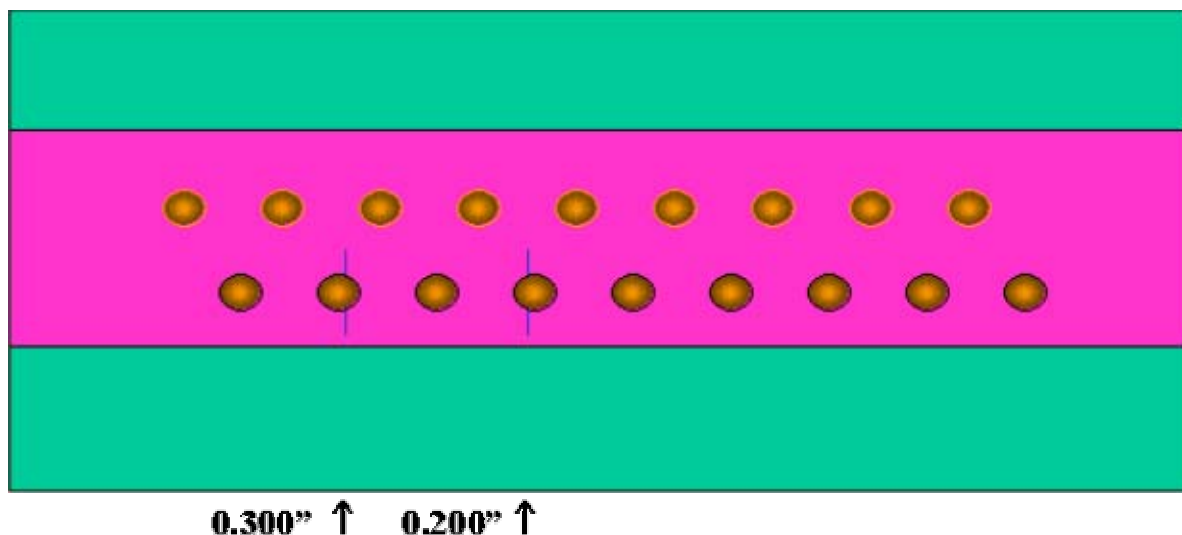


Figure 14. Sample used for initial performance demonstration of 64-element array: (Note: The wider upper layer has fastener holes with countersinks. The narrower lower layer has holes without countersinks. The four lines represent through cracks in the lower layer. The cracks on the second hole from the left are 0.300" each, and those on the fourth hole from the left are 0.200" each.)

The sample was scanned in the short dimension, with the scanning indexed along the long dimension of the sample. In the first scan, a frequency of 160Hz was used. This corresponds to a skin depth of around 0.5 inch. The excitation current was parallel to the long dimension of the sample, and thus normal to the cracks. The current launched into the surface of the sample was 90 milliamps. The phase was adjusted until the flaws were easily seen. This is a relatively simple and quick process, since the array images a sufficient swath across the sample to see the flaw response in only one or two passes.

When the flaws were well detected, a scan was taken and an image stored. The image was stored both as the raw image from the "un-massaged" data, and from data that had been "contrast squeezed" from 250 parts down to 219 parts. The data appear in Figure 15 as two crescents for each of the fastener holes, with the crescents accented where the flaws are located. It is easy to see both of the flaws. The reason for the crescents is that the current is unidirectional, and where it intersects the fastener hole tangentially, it is more cramped together than where it intersects it

radially. The regions where the flaws are show a clear enhancement and widening of the normal crescent response.

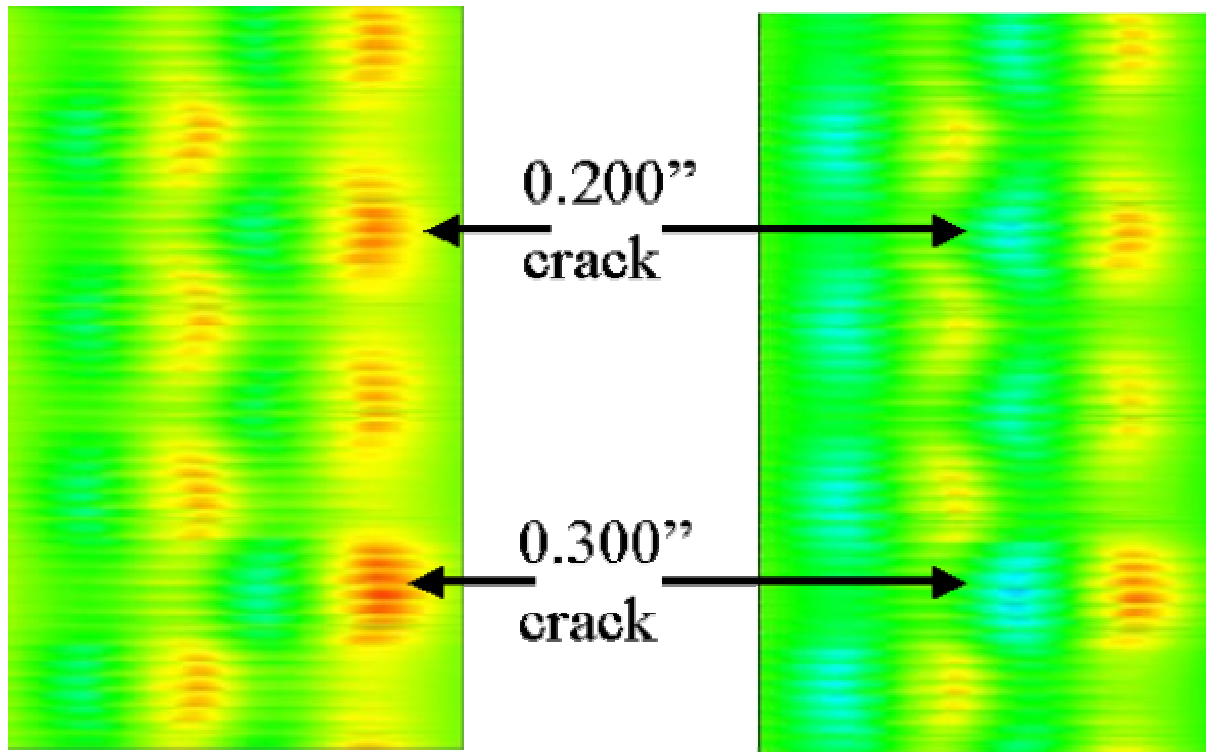


Figure 15. 64-element scan of sample shown in Figure 14: The array is operated in magnetometer mode. The sample is rotated 90 degrees from its image in the previous figure. The 0.300 and 0.200 flaws are easily seen in both images, but the contrast squeezed image on the right picks out the inside flaws slightly better. All of the fastener holes are detected as a pair of crescents. Only two of the fastener holes have flaws.

The images in figure 15 reveal “bands” that go left and right through the data. These are due to the fact that each of the strings is spread across the conducting ribbons in the launcher instead of parallel to them. So from one end of the string to the other, approximately 0.8 inches across the width of the launcher is covered. This results in a somewhat different amount of residual excitation field for each of the sensors in the string, as can be seen by the stripes. The stripes actually show the position and width of each of the strings.

We are working on minimizing this effect. It is due to the fact that as you move out from the symmetry center of the launcher, the asymmetry of the field increases, as a result of the fact that there are more conductors on one side of the location than on the other. Sensors located further from the center are driven more closely to their non-linear and hence less sensitive regime. For applications where it is preferable to launch the current parallel to the scan direction, then the launcher current ribbons are essentially parallel to the strings, and the net effect is larger, but on

any given string it is smaller, so that the striping is gradated across the image, and slightly greater in its effect.

In order to demonstrate the use of the spatial gradient of the field, we scanned a similar sample with several 0.600" flaws. This sample was not used to demonstrate sensitivity, but rather over all function. The sample is the same as shown in figure 14, with the exception that the flaws are somewhat larger, and not on both sides of all fastener holes. It is shown in Figure 16.

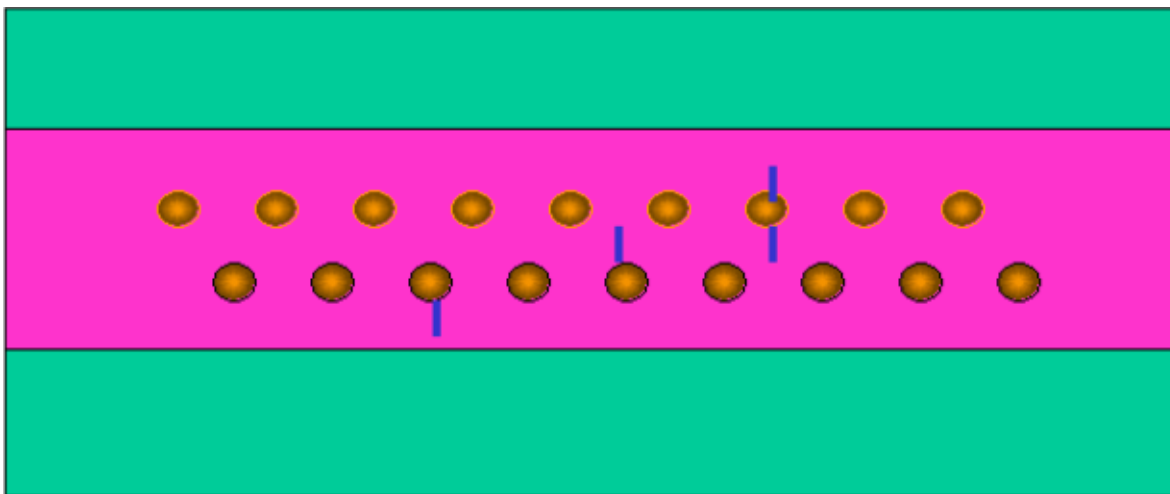


Figure 16. Sample used to demonstrate functionality of field gradient as a viable scanning parameter. All of the flaws are 0.600" in length, and some are only on one side of the fastener hole; otherwise, the sample is identical to that of Figure 14.

Figure 17 shows a gradiometer scan of the sample shown in Figure 16. The flaws are all clearly seen as the darker patches. What is interesting about this example scan, is that the fastener holes are hardly seen. This is due to the fact that the gradient is calculated as a difference of signals between adjacent sensors, thereby eliminating what is the same in each from contributing to the image. This gives "hope" that with a properly devised subtraction process, the signatures due to the fastener holes could potentially be all but completely eliminated.

Using drive currents of two different frequencies, each with phases adjustable with respect to zero degrees, and each with adjustable amplitude, holds promise for elimination of the fastener hole signatures. If the signals resulting from the two frequencies are each separately demodulated from the MR sensor outputs, then a careful treatment of them in software may just do the trick. The signal at the higher frequency or the unnecessary phase would be multiplied by some number between 0.01 and 1.00, and then subtracted from that at the frequency (or phase) of interest, and the result passed on to the imaging software to be displayed. Judicious adjustment of the frequency, amplitude, phase, and finally the subtracted fraction of the signal not containing the flaw data should produce the desired elimination of the fastener hole signature.



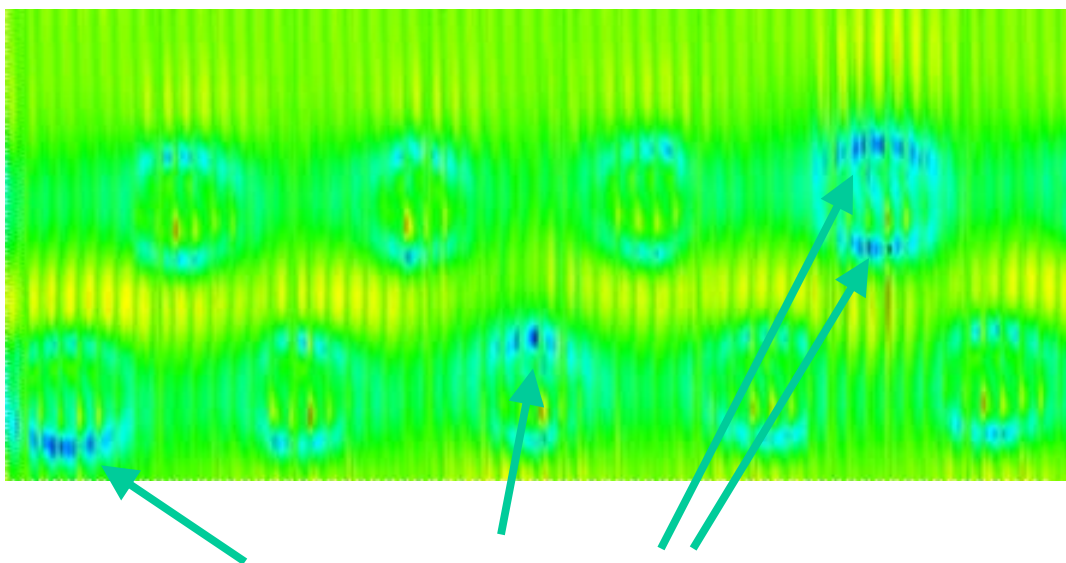


Figure 17. Gradiometer scan image of the sample in Figure 16: All of the cracks are seen, as indicated by the arrows, and the fastener holes are not pronounced. This scan was not processed in any way, but is shown as taken.

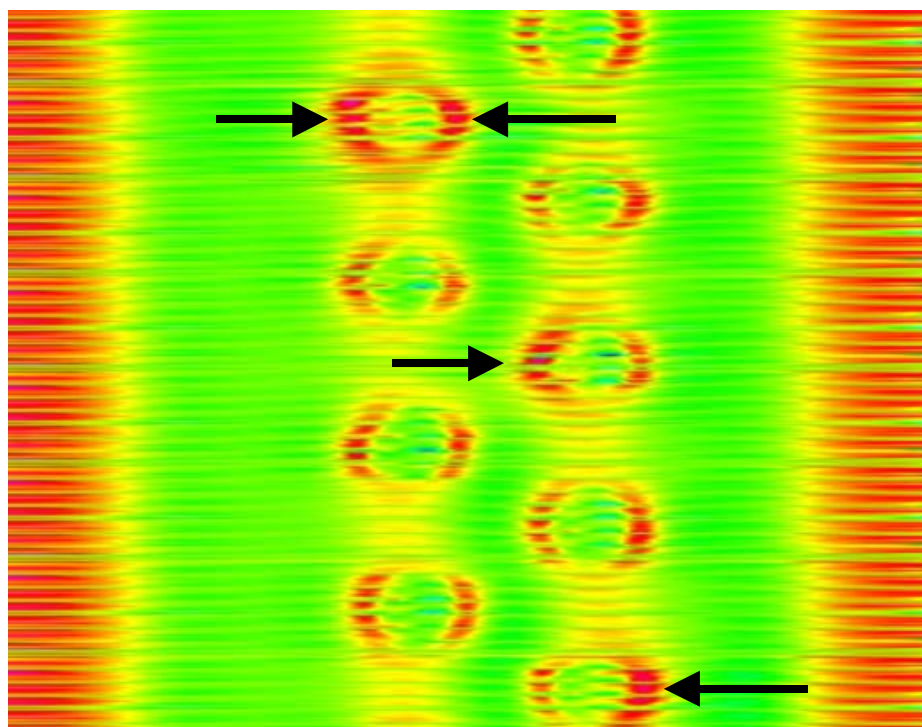


Figure 18. Wider gradiometer scan of the same sample, rotated by ninety degrees: Arrows show flaws, and the bands at sides show the edge of the narrower lower layer.



Figure 18 shows another gradiometer plot of a larger portion of the same sample. The sample is shown rotated clockwise by ninety degrees from the scan in Figure 17. It is also taken at one hundred eighty degrees of phase difference from Figure 17. This scan serves to show that some other features show up well with the gradiometer scan. These include the two bands along each side of the scan, which define the edges of the lower narrower plate.

## **5.0 CONCLUSIONS**

The 64-element imaging array has been built, and preliminary tests show that it performs as expected. We have successfully detected deeply lying flaws in thick aluminum structure. Although there are a number of technical issues still remaining to be resolved, none are “show-stoppers”, and we expect full routine optimized operation is easily achievable. The biggest remaining issue is that of comparison of the performance of the array with a similar one composed of GMR sensors, and, if practical or appropriate, SDT sensors as well. We see the 64-element array as a useful “test bed” for further work in arriving at the recommended configuration for the prototype MR sensor array for Air Force depot inspections, and field NDE.